ACS Photonics

pubs.acs.org/journal/apchd5 Article

Absorption-Based Diamond Spin Microscopy on a Plasmonic Quantum Metasurface

Laura Kim,* Hyeongrak Choi, Matthew E. Trusheim, and Dirk R. Englund*

Cite This: *ACS Photonics* 2021, 8, 3218–3225 Read Online

ACCESS | Metrics & More | Article Recommendations | Supporting Information

ABSTRACT: Nitrogen vacancy (NV) centers in diamond have emerged as a leading quantum sensor platform, combining exceptional sensitivity with nanoscale spatial resolution by optically detected magnetic resonance (ODMR). Because fluorescence-based ODMR techniques are limited by low photon collection efficiency and modulation contrast, there has been growing interest in infrared (IR)-absorption-based readout of the NV singlet state transition. IR readout can improve contrast and collection efficiency, but it has thus far been limited to long-path length geometries in bulk samples due to the small absorption cross section of the NV singlet state. Here, we propose to amplify the IR absorption by introducing a resonant diamond metallodielectric metasurface that concentrates the optical field near the diamond surface. This "plasmonic quantum sensing metasurface" (PQSM) supports plasmonic surface lattice resonances and achieves desired balance between field localization and sensing volume to optimize spin readout sensitivity. From combined electromagnetic and rate-equation modeling, we estimate a near-spin-projection-noise-limited sensitivity below 1 nT $Hz^{-1/2}$ per μm^2 of sensing area using numbers for present-day NV diamond samples and fabrication techniques. The proposed PQSM enables a new form of microscopic ODMR sensing with infrared readout near the spin-projection-noise-limited sensitivity, making it appealing for the most demanding applications such as imaging through scattering tissues and spatially resolved chemical NMR detection.

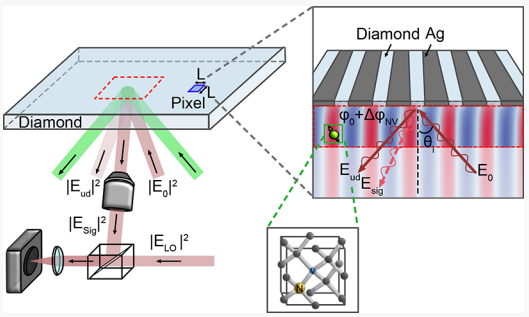

KEYWORDS: *quantum sensing, nitrogen vacancy center, color centers, diamond quantum microscopy, plasmonics, metasurfaces*

The ability to optically measure quantities such as electric field, magnetic field, temperature, and strain under ambient conditions makes the nitrogen vacancy (NV) system appealing for a range of wide-field sensing applications from imaging biological systems[1] and electrical activity in integrated circuits[2] to studying quantum magnetism and superconductivity in quantum materials.[3−6] NV-based magnetometers have shown exceptional sensitivity at room temperature, but conventional fluorescence-based readout methods result in sensitivity values far from the spin projection noise limit primarily due to background fluorescence, poor photon collection efficiency, and low spin-state contrast.[7] These limitations can be overcome by probing the infrared (IR) singlet transition near 1042 nm by absorption.[8] However, this absorption-based readout has only been demonstrated for bulk diamond samples with a large optical path length of millimeters[9,10] to centimeters[11,12] due to the small absorption cross section of the singlet state transition. This long pathlength requirement presents the central challenge in IR readout to imaging microscopy, where the sensing depth should commonly be below the micrometer scale. The plasmonic quantum sensing metasurface (PQSM) solves this problem by confining vertically incident IR probe light in a micrometer-thick NV layer with a quality factor near 300. The PQSM consists of a metallodielectric grating that couples plasmonic surface lattice excitations with Bragg modes,[13,14] caused by the Rayleigh−Wood anomaly (RWA). Unlike fluorescence, the directional reflection (or transmission) can be captured with near-unity efficiency. In particular, detection of the reflected coherent probe light with a standard camera enables shot-noise limited detection, eliminating the need of single photon detectors. Taken together, our analysis predicts that the PQSM coupled to NV sensing layers can enable a sensitivity below 1 nT $Hz^{-1/2}$ per μm^2 of sensing area.

RESULTS

IR-Absorption-Based Detection Scheme. The principle of NV-based magnetometers lies in the Zeeman energy shift of the NV defect spin sublevels that can be polarized and measured optically. As illustrated in Figure 1a, the spin sublevels $m_s = 0$ and $m_s = \pm 1$ of the $^3A_2$ ground triplet state, labeled as $|1\rangle$ and $|2\rangle$, respectively, are separated by a zero-field

Received: July 5, 2021
Published: November 4, 2021

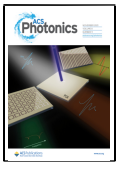

https://doi.org/10.1021/acsphotonics.1c01005
ACS Photonics 2021, 8, 3218–3225

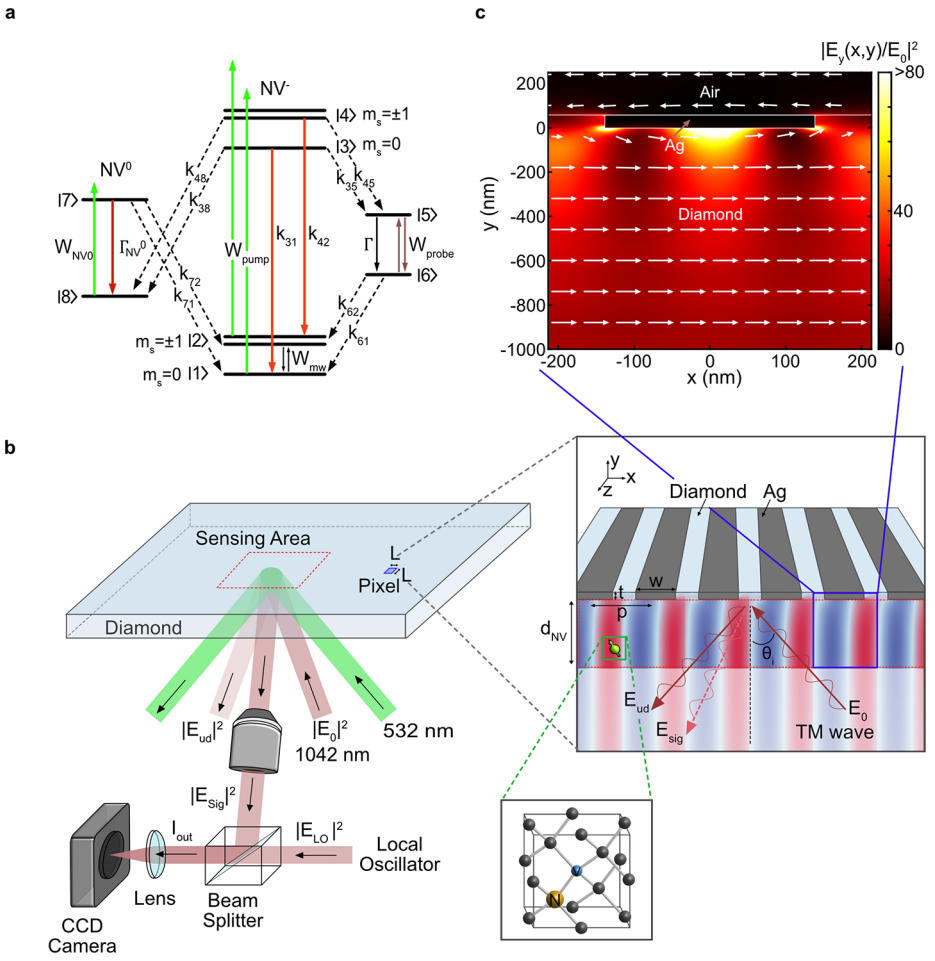

Figure 1. (a) Energy-level diagram for negatively charged and neutral nitrogen NV centers in diamond. (b) Absorption-based diamond spin microscopy on a PQSM consisting of an embedded metallodielectric grating structure. TM-polarized incoming light excites a plasmonic SLR mode, creating a vertically extended field profile. Upon an applied microwave magnetic field with a Rabi frequency of Ω_R, the NV spin response is manifested as phase and amplitude changes in E_{sig}. The spin-dependent signal, $|E_{sig}|^2$, is separated from the undiffracted beam, $|E_{ud}|^2$, in a dark-field excitation geometry and interferes with a local oscillator, $|E_{LO}|^2$. The interfered output beam, I_{out}, is detected by a CCD camera. (c) Total electric field intensity profile at λ_s = 1042 nm with p = 426.5 nm, w = 277 nm, t = 55 nm, and θ_i = 1°. The arrow plot shows the magnetic field, $\vec{B}$, generated by a uniform driving current in an array of plasmonic silver wires. The lengths of the arrows are proportional to the magnetic field strength. The structure is assumed to be infinitely periodic in the x-direction.

splitting of D = 2.87 GHz, whose transition can be accessed with a resonant microwave field. Upon spin-conserving off-resonant green laser excitation, a fraction of the population decays nonradiatively into the $^1A_1$ metastable singlet state, $|5\rangle$, predominantly from $|4\rangle$ as $k_{45} \gg k_{35}$, where k_{ij} indicates the decay rate from level i to level j. After a sub-nanosecond decay from $|5\rangle$ to $|6\rangle$, the shelving time at $|6\rangle$ exceeds 200 ns at room temperature.[15] Therefore, the population of $|6\rangle$ can be measured by absorption of the singlet state transition, $|6\rangle \rightarrow |5\rangle$, resonant at 1042 nm.

Figure 1b shows the proposed quantum diamond microscopy together with the PQSM. The PQSM is pumped with a green laser at λ_t = 532 nm with intensity of I_t for NV spin initialization, and it is back-side illuminated with transverse magnetic (TM) polarized probe light at an angle, θ_i, at λ_s = 1042 nm with intensity of I_s for IR readout. Upon IR incidence, the light field is localized and intensified near the sensing surface, providing a sufficient field overlap with the NV layer with thickness, d_{NV}. The PQSM-NV signal is manifested as spin-dependent phase and amplitude changes in the IR reflection. The signal field, E_{sig}, is separated from the undiffracted field, E_{ud}, in a dark-field excitation geometry (i.e., k-vector filtering). Unlike fluorescence measurement, in this absorption-based measurement scheme, the spatially well-defined signal beam ensures a near-unity collection efficiency. The collected signal beam is interfered with the local oscillator, E_{LO}. Phase-sensitive homodyne detection is performed by detecting the interfered light intensity, I_{out}, given by eq 1, with a CCD camera for wide-field imaging.

$$\frac{I_{out}(I_t, \Omega_R, R, \Delta\phi_{LO})}{I_s} = (1 - R) + R|r(I_t, \Omega_R)|^2 + 2\sqrt{(1 - R)R}\,|r(I_t, \Omega_R)|\cos(\Delta\phi_{LO} + \Delta\phi_{NV}(I_t, \Omega_R)) \quad (1)$$

where R is the power splitting ratio of the beam splitter, $r(I_t, \Omega_R)$ is the complex reflection coefficient of the PQSM, $\Delta\phi_{LO}$ is the relative phase difference between E_{LO} and E_{sig} when I_t = 0, and $\Delta\phi_{NV}$ is the additional phase change of E_{sig} incurred by the NV spin response. A combination of R and $\Delta\phi_{LO}$ is chosen to maximize the signal-to-noise ratio (SNR) of the PQSM. The embedded metallic array of the PQSM doubles as a wire array

https://doi.org/10.1021/acsphotonics.1c01005
ACS Photonics 2021, 8, 3218−3225

for NV microwave control:[16,17] with a subwavelength spacing, an array of the silver wires produces a homogeneous transverse magnetic field, $\vec{B}$, as shown in Figure 1c. Local excitation and probing of NVs within a pixel are possible by running a current through an individual wire. The plasmonic arrays may also enable subpixel addressing of emitters by creating a magnetic field gradient.[18]

Metasurface Design. Here we discuss photonic design criteria to maximize the IR signal of spin ensemble sensors. The IR absorption readout has only been successfully implemented with bulk diamond samples due to the intrinsic absorption cross sectional area that is about an order of magnitude smaller than that of the triplet state transition (i.e., $|1\rangle \rightarrow |3\rangle$ and $|2\rangle \rightarrow |4\rangle$).[9,12] Resonant structures can enhance this weak light−NV interaction by modifying the local electromagnetic environment of NV quantum sensors. The rate of absorption of a NV center under an oscillating electromagnetic field with frequency, ω_s, can be expressed following Fermi's golden rule.

$$\Gamma_{abs} = \frac{2\pi}{\hbar}|\langle 5|\vec{\mu}\cdot\vec{E}|6\rangle|^2\rho(\omega_s) \tag{2}$$

where $\vec{\mu} = e\cdot\vec{r}$ is the transition dipole moment operator, $\vec{E}$ is the electric field, and $\rho(\omega) = \frac{1}{\pi\hbar}\frac{\frac{1}{2}\gamma^*}{(\omega-\omega_s)^2+\left(\frac{1}{2}\gamma^*\right)^2}$ is the electronic density of states, which is modeled as a continuum of final states with a Lorentzian distribution centered at ω_s with linewidth γ^*. For a given angle, β, between the NV quantum sensor's transition dipole orientation, $\vec{\mu}$, and the electric field, $\vec{E}$, created by the PQSM, eq 2 can be expressed as eq 3 in terms of the spontaneous emission rate of the singlet state transition, $\gamma = \frac{\omega_s^3|\langle 5|\vec{\mu}|6\rangle|^2}{3\pi\epsilon\hbar c^3}$.

$$\Gamma_{abs} = \frac{3}{\pi^2\hbar}\frac{\gamma}{\gamma^*}\left(\frac{\lambda_s}{\sqrt{\epsilon}}\right)^3\cdot\frac{1}{2}\epsilon_0\epsilon|\vec{E}|^2\cos^2(\beta) \tag{3}$$

where ϵ is the relative permittivity of diamond. The rate of transition enhancement originates from the electric field intensity enhancement at the position of a NV quantum sensor, assuming the properties of the sensor remain unperturbed by the PQSM. Contributions of all four orientations of NV emitters are averaged, and the ensemble response is spatially integrated to determine the signal of the PQSM.

To guide the PQSM optimization, we adopt a figure of merit (FOM) maximizing the NV spin-dependent SNR for a given sensing volume of $V_{pixel} = L^2 \times d_{NV}$, where L^2 is the area of a pixel and d_{NV} is the thickness of the NV layer with a uniform density of n_{NV}. The SNR of the pixelated plasmonic imaging surface is given by eq 4 under the assumption of the shot noise limit.

$$\begin{aligned}\mathrm{SNR} &= \frac{|N_0 - N_1|}{\sqrt{N_0 + N_1}} \\ &= \sqrt{\frac{\Delta t_{mea}L^2}{\hbar\omega_0}}\frac{I(0) - I(\Omega_R)}{\sqrt{I(0) + I(\Omega_R)}}\end{aligned} \tag{4}$$

where N_0 and N_1 are the average numbers of photons detected from the $m_s = 0$ and $m_s = \pm 1$ states, respectively, per measurement, Δt_{mea} is the total readout time, and $I(0/\Omega_R) = I_{out}(I_t, 0/\Omega_R, R, \Delta\phi_{LO})$. Here, we define $|r(I_t, \Omega_R)|$ as $|\alpha_0 - \alpha_{NV}(I_t, \Omega_R)|$, where $|\alpha_0|^2$ is the intrinsic reflection of the PQSM (when $I_t = 0$ and $\alpha_{NV} = 0$) and $|\alpha_{NV}(I_t, \Omega_R)|^2 = A_{NV}$ is the NV absorption. For $|\alpha_0|^2 \gg |\alpha_{NV}(I_t, \Omega_R)|^2$, the SNR scales with $|\alpha_{NV}(I_t, \Omega_R)| - |\alpha_{NV}(I_t, 0)|$; equivalently, it scales with $\sqrt{\langle|E/E_0|^2\rangle V_{pixel}n_{NV}}$, where $\langle|E/E_0|^2\rangle = \int_{pixel}|E/E_0|^2\,dV/\int_{pixel}dV$ is the spatially averaged optical field enhancement factor over the single-pass field without plasmonic enhancement, E_0. We choose this quantity as a FOM to optimize the PQSM. The detailed derivation for this FOM is described in SI Section 3.

Localized surface plasmon (LSP) resonances can focus light intensity at subwavelength scales and have been used to increase spontaneous emission rates of single emitters or ensembles of emitters confined in a nanometer-scale volume.[19−27] However, this field concentration comes with the trade-off of reducing the number of NV centers, N_{NV}, that are coupled to the optical field. In addition, such field concentration near a metallic material leads to losses due to Ohmic damping and dephasing. Here we delocalize field while maintaining a large electric field intensity and mitigate losses via coupling LSP resonances to the diffractive states of RWA. Balancing this trade-off depends on the use case. Increasing d_{NV} beyond the thickness of the sample being probed improves signal only marginally while adding shot noise (refer to Section 3 of the SI for detailed discussion). This argument applies in the lateral direction. Therefore, if a sample is micrometer-scale, a RWA-like mode that has a better electric field overlap with a thicker d_{NV} would be more advantageous. On the other hand, studying, for example, atom-thick quantum materials[6] would benefit from LSP-like optical modes with small confinement. The electric field intensity profile shown in Figure 1c is the result of an optimization with FOM being the electric field intensity spatially averaged over a given NV layer thickness of 1 μm under a plane wave excitation.

The PQSM consists of a periodic arrangement of plasmonic structures embedded in diamond that satisfies the dispersion relation given by eq 5.

$$\frac{\omega_s}{c}n = |k_x + mG| \tag{5}$$

where c is the speed of light in vacuum, n is the refractive index of diamond, $k_x = k_0\sin(\theta_i)$ is the momentum component of free-space light in the direction of the grating period, m denotes the diffraction order, and $|G|$ is given by $2\pi/p$.[13,14] An incoming far-field radiation with momentum, k_0, gains momentum by integer multiples of $|G|$ and can satisfy momentum matching conditions to couple with the grating mode. When the Bragg scattering condition is met, the incident electromagnetic wave diffracts parallel to the grating surface and creates a field profile that extends vertically away from the grating surface,[28,29] providing a sufficient field overlap with the NV layer. The large field concentration near the surface is accompanied when the RWA is coupled with the periodic array of plasmonic structures that support a surface lattice resonance (SLR). The RWA mode alone is independent of the material property of the embedded plasmonic structures (eq 5). However, the mode shown in Figure 1b shows plasmonic nature as it is highly dependent on the permittivity of the metallic material. When silver is replaced with a perfect electric conductor, which supports no plasmonic resonance as no field penetration is possible to excite collective oscillations of free carriers, a dramatic field intensity reduction is observed

https://doi.org/10.1021/acsphotonics.1c01005
ACS Photonics 2021, 8, 3218−3225

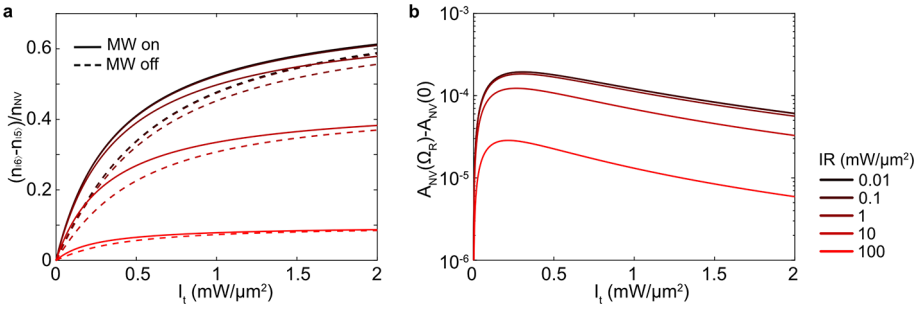

Figure 2. (a) Normalized net population of the ground singlet state, $(n_{|6\rangle}- n_{|5\rangle})/n_{NV}$, as a function of I_t with (solid) and without (dotted) an applied microwave field. (b) Differences in NV absorption, A_{NV}, with and without an applied MW field excitation.

(refer to SI Section 1). The SLR of the proposed PQSM achieves Q near 300. The PQSM combines a large field enhancement of the LSP mode and delocalization of the Bragg mode, making the SLR well-suited for ensemble-based sensing. Furthermore, the same PQSM structure can accommodate a Bragg mode resonant at λ_t = 532 nm with a change in incidence angle with $\langle|E/E_0|^2\rangle$ approximately 2 (refer to SI Section 1).

Metasurface Spin-Dependent Response. The photodynamics of the NV system is captured with the 8-level energy structure that accounts for photoionization as shown in Figure 1a. The local density of each sublevel, $n_{|i\rangle}$, is calculated based on the coupled rate equations described in SI Section 2. The spin-dependent IR absorption is then obtained from the calculated net population of the ground singlet state. In this work, we base our calculations on the properties of an NV layer in a diamond chip that are characterized in ref 30; a 1 μm thick NV layer with a density of 2 ppm is assumed. For a [100] diamond plane, all four orientations of NVs are expected to have equal contributions for the given SLR-induced field profile.

To account for stimulated emission, we consider a net population of the ground singlet state, $n_{|6\rangle} - n_{|5\rangle}$. Under steady state conditions (in the case of continuous wave (CW)-ODMR), $n_{|6\rangle} - n_{|5\rangle}$ weakly depends on the IR probe intensity, I_s, until the absorption rate becomes comparable to the excited state decay rate (Figure 2a). Because the lifetime of the ground state, $|6\rangle$, is approximately two orders of magnitude longer than that of the excited state, $|5\rangle$,[15] the singlet state transition (i.e., $|6\rangle \leftrightarrow |5\rangle$) has an exceptionally high saturation intensity, enabling each NV to absorb multiple photons per cycle. Resonant structures make the sensing surface more power-efficient; the IR incident intensity that brings the system to this saturation level is effectively reduced by a factor of $\sim\langle|E/E_0|^2\rangle$.

The PQSM resonant field intensity enhancement also modifies the radiative decay rate by $\gamma_{rad} \rightarrow F_p\gamma_{rad} + \gamma_q$, where F_p is the Purcell factor and γ_q is the rate of quenching. However, the probability of absorbed IR photons to re-emit is negligible for the following reasons. First, the singlet state transition shows a low intrinsic quantum efficiency, $\frac{\gamma_{rad}}{\Gamma}$, near 0.1%.[31] Second, the quality factor of the NV's singlet state transition at room temperature is orders of magnitude smaller than that of the PQSM. Regarding quenching, as quenching is a short-range phenomenon, it is expected to have minimal effects on the overall photodynamics considering the micrometer-scale SLR. In addition, this nonradiative channel is considered a loss and is detrimental in fluorescence measurements. However, this effect may be a benefit for the absorption-based readout because it contributes to resetting electrons back down to the ground state, $|6\rangle$, more quickly, thus making more electrons available to absorb incoming photons at 1042 nm. Upon an applied microwave field, electron spins from the excited $m_s = \pm1$ states preferentially decay into the singlet states (i.e., $k_{4S} \gg k_{3S}$). This incurs an increase in spin-selective NV IR absorption (i.e., $|\alpha_{NV}(I_t, \Omega_R)|^2 > |\alpha_{NV}(I_t, 0)|^2$). The change in NV absorption with and without an applied MW field is shown in Figure 2b. Due to the Kramers−Kronig relations, NV absorption accompanies a spin-dependent phase shift, $\Delta\phi_{NV}(I_t, \Omega_R)$. The spin-dependent phase and amplitude modulations of the reflected IR probe field are the key capabilities of the PQSM that enable quantum sensing. These phase and amplitude changes of the IR signal allow for a phase-sensitive measurement. Here, we implement a phase-sensitive coherent homodyne detection, where a local oscillator interferes with the spin-dependent signal from the PQSM. Under the conditions considered in this work, the photon shot noise dominates, and a better SNR is achieved by biasing the interferometric readout with a controlled phase difference. SI Section 4 provides analytical forms for the SNR under homodyne and direct detection. Furthermore, SI Section 4 provides detail in Supporting Information Figure 5c that the local oscillator can be biased to achieve unity spin contrast. Homodyne detection is particularly advantageous for fast imaging on focal plane arrays. Under confocal scanning, for example, a focal plane array could be integrated into an integrated photonics layer[32] or programmable photonic unitaries;[33] this would also enable basis transformations for compressive sampling and super-resolution imaging.[34−36] Furthermore, coherent detection also enables quantum enhanced imaging schemes such as "interaction-free" imaging,[37] imaging with undetected photons,[38] or loss-tolerant quantum absorption measurements.[39]

DISCUSSION

DC Sensitivity. The shot-noise-limited sensitivity of a CW-ODMR-based magnetometer per root area based on IR absorption measurement is given by eq 6.

$$\eta_{CW}^{A} = \frac{\hbar\Gamma_{MW}}{g\mu_B}\frac{\sqrt{\Delta t_{mea}L^2}}{SNR} \tag{6}$$

where $g \approx 2.003$ is the g-factor of of the electron of the NV center, μ_B is the Bohr magneton, and Γ_{MW} is the magnetic-resonance linewidth which can be approximated as $\Gamma_{MW} = 2/T_2^*$, assuming no power broadening from pump or microwaves. The sensitivity is normalized by an arbitrary pixel area, L^2, and is reported for a given NV layer thickness of d_{NV} = 1 μm and a

https://doi.org/10.1021/acsphotonics.1c01005
ACS Photonics 2021, 8, 3218−3225

given NV density of 2 ppm. The remaining experimental parameters are listed in Table 1. An alternative magnetometry

Table 1. Physical Parameters Used in This Work

parameter	value
$k_{31} = k_{42}$	66 μs^{-1} (ref 41)
k_{35}	7.9 μs^{-1} (ref 41)
k_{45}	53 μs^{-1} (ref 41)
k_{61}	1 μs^{-1} (ref 41)
k_{62}	0.7 μs^{-1} (ref 41)
$k_{38} = k_{48}$	41.8 MHz/mW (ref 41)
$k_{71} = k_{72}$	35.5 MHz/mW (ref 41)
Γ	1 ns^{-1} (ref 15)
Γ_{NV^0}	53 μs^{-1} (refs 41, 42)
σ_t	3×10^{-21} m^2 (ref 43)
σ_s	3×10^{-22} m^2 (refs 9, 12)
σ_{NV^0}	6×10^{-21} m^2 (refs 41, 42)
n_{NV}	2 ppm (ref 30)
T_2^*	1 μs (ref 30)
T_2	10 μs (refs 7, 30)

method to CW-ODMR, such as pulsed ODMR or Ramsey sequences, can be exploited to achieve T_2^*-limited performance. It is useful to compare the photon-shot-noise-limited sensitivity with the spin-projection-noise-limited sensitivity of a magnetometer consisting of noninteracting spin ensemble, given by eq 7

$$\eta_{sp}^{A,\text{ensemble}} = \frac{\hbar}{g\mu_B\sqrt{n_{NV}d_{NV}\tau}} \tag{7}$$

where τ is the free precession time per measurement. Figure 3 shows that the PQSM can achieve sub-nT $Hz^{-1/2}$ sensitivity

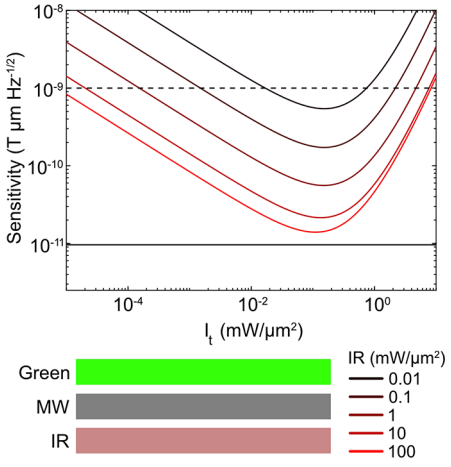

Figure 3. (a) Area-normalized sensitivity as a function of I_t with varying I_s. The dotted black line indicates 1 nT $Hz^{-1/2}$ sensitivity for a 1 μm^2 sensing area. The solid black line indicates the spin-projection-noise-limited sensitivity.

per μm^2 sensing surface area. The sensitivity improves with increasing green laser intensity until two-photon-mediated photoionization processes start to become considerable. With an IR intensity approaching 100 mW/μm^2, the sensitivity becomes only a factor of approximately 1.45 away from the spin-projection-noise-limited sensitivity. The calculations suggest that sub-nT $Hz^{-1/2}$ sensitivity can be maintained under wide-field illumination with reasonable excitation powers (e.g., 1 W of green and 100 mW of IR over 100 $\mu m \times 100$ μm sensing area). A better sensitivity can be achieved with an increase in the NV density without compromising the spin properties via realizing a higher NV conversion efficiency. Additionally, a further improvement is possible by implementing a decoupling sequence that is compatible with dc magnetometry to protect NV sensors from dephasing mechanisms, and it has been experimentally demonstrated that such method can extend the T_2^* up to 10 μs.[40]

AC Sensitivity. Sources of the NV spin dephasing can be largely eliminated with coherent control techniques such as the Hahn echo sequence. With an added π-pulse halfway through the interrogation time, a net phase accumulated due to a static or slowly varying magnetic field cancels out, and the interrogation time can be extended to a value of $\sim T_2$. Thus, the AC sensitivity can improve by a factor of approximately $\sqrt{T_2^*/T_2}$ at the cost of a reduced bandwidth and insensitivity to magnetic field with an oscillating period longer than T_2. For a given NV density of 2 ppm, T_2 is about an order of magnitude longer than T_2^*.[7,30] The sensitivity per root area for an ensemble-based AC magnetometer is given by eq 8.[7]

$$\eta_{a.c.}^{A} = \frac{\hbar\sigma_R e^{\tau/T_2}}{g\mu_B\sqrt{n_{NV}d_{NV}\tau}}\sqrt{1 + \frac{t_I + \Delta t_{mea}}{\tau}} \tag{8}$$

where T_2 is the characteristic dephasing time, t_I is the initialization time, and σ_R is the readout fidelity. The rate equations are solved as a function of time to obtain time-dependent population evolution as shown in Figure 4a. The system achieves maximum spin contrast approximately within the first 1 μs of readout and finally loses polarization with increasing readout time, limited by the lifetime of the ground singlet state. For given I_t and I_s, an optimal readout time that maximizes the time-integrated signal is calculated (refer to SI Section 5). The optimal readout time is found based on the balance between maintaining a spin contrast and preventing a large measurement overhead time. An additional shot noise introduced by the optical readout is quantified with the parameter σ_R (eq 9), which is equivalent to an inverse of readout fidelity.[7]

$$\sigma_R = \sqrt{1 + \frac{2(a+b)}{(a-b)^2}} \tag{9}$$

where a and b are the average numbers of photons detected from the $m_s = 0$ and $m_s = \pm 1$ states per spin per measurement, respectively. As shown in Figure 4 b, the PQSM achieves near unity readout fidelity per shot. Figure 5 shows the AC sensitivity down to $\sim$10 pT $Hz^{-1/2}$ per 1 μm^2 sensing surface area.

CONCLUSION

In summary, we report a diamond quantum sensing surface consisting of embedded plasmonic nanostructures, which shows a sub-nT $Hz^{-1/2}$ sensitivity per a 1 μm^2 sensing surface. This exceptional performance is achieved by the SLR that optimizes an electric field enhancement within a micrometer-scale NV layer. The plasmonic structures of the PQSM also provide an optimal microwave control by generating a homogeneous magnetic field across a large sensing area. Combined with a homodyne detection, the PQSM makes a new type of quantum microscope that enables high-speed imaging measurements at photon shot noise limit.

https://doi.org/10.1021/acsphotonics.1c01005
ACS Photonics 2021, 8, 3218−3225

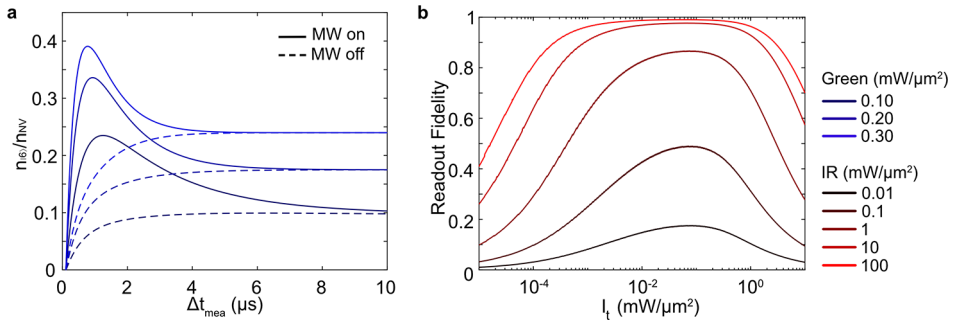

Figure 4. (a) Normalized population of the ground singlet state with (solid) and without (dotted) an applied microwave field as a function of readout time for a given I_s = 1 mW/μm^2. (b) Readout fidelity as a function of I_t with varying I_s.

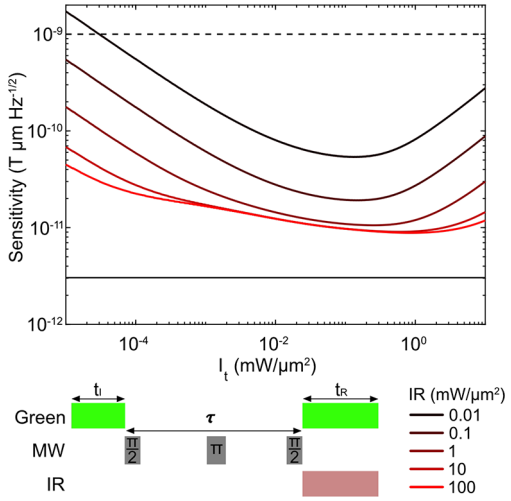

Figure 5. AC sensitivity per root sensing surface area as a function of I_t with varying I_s. The solid black line indicates the spin-projection-noise-limited sensitivity.

This PQSM has far-reaching implications in quantum science. The metasurface-coupled quantum sensor arrays can enable manipulation of accumulated phase and polarization at each position of a quantum sensor. By superposing spin-dependent reflection or transmission, it may even be possible to entangle different regions of the metasurface. The entangled quantum metasurface is useful in applications that demand measurements of correlated quantum fluctuation such as quantum spin liquids in quantum materials.[44,45] Such an approach can exploit entanglement-enhanced quantum sensing protocols to achieve performance beyond the standard quantum limit.[46,47]

■ ASSOCIATED CONTENT

Supporting Information

The Supporting Information is available free of charge at https://pubs.acs.org/doi/10.1021/acsphotonics.1c01005.

More information about the silver-diamond metallodielectric grating structures, rate equations for the 8-level scheme, SNR of the PQSM, optimization of homodyne detection, and optimal readout conditions for pulsed measurements (PDF)

■ AUTHOR INFORMATION

Corresponding Authors

Laura Kim − *Research Laboratory of Electronics, Massachusetts Institute of Technology, Cambridge, Massachusetts 02139, United States*; Email: lbkim@mit.edu

Dirk R. Englund − *Research Laboratory of Electronics, Massachusetts Institute of Technology, Cambridge, Massachusetts 02139, United States; Department of Electrical Engineering and Computer Science, Massachusetts Institute of Technology, Cambridge, Massachusetts 02139, United States;* orcid.org/0000-0002-1043-3489; Email: englund@mit.edu

Authors

Hyeongrak Choi − *Research Laboratory of Electronics, Massachusetts Institute of Technology, Cambridge, Massachusetts 02139, United States; Department of Electrical Engineering and Computer Science, Massachusetts Institute of Technology, Cambridge, Massachusetts 02139, United States*

Matthew E. Trusheim − *Research Laboratory of Electronics, Massachusetts Institute of Technology, Cambridge, Massachusetts 02139, United States; Sensors and Electron Devices Directorate, U.S. Army Research Laboratory, Adelphi, Maryland 20783, United States*

Complete contact information is available at: https://pubs.acs.org/10.1021/acsphotonics.1c01005

Notes

The authors declare no competing financial interest.

■ ACKNOWLEDGMENTS

L.K. acknowledges support through an appointment to the Intelligence Community Postdoctoral Research Fellowship Program at the Massachusetts Institute of Technology, administered by Oak Ridge Institute for Science and Education through an interagency agreement between the U.S. Department of Energy and the Office of the Director of National Intelligence. H.C. acknowledges support through Claude E. Shannon Fellowship and the DARPA DRINQS, D18AC00014 program. M.E.T. acknowledges support through the Army Research Laboratory ENIAC Distinguished Postdoctoral Fellowship. D.R.E. acknowledges support from the Bose Research Fellowship, the Army Research Office Multidisciplinary University Research Initiative (ARO MURI) biological transduction program, and the NSF CUA. We thank Dr. Jennifer Schloss and Jordan Goldstein for helpful discussions.

REFERENCES

(1) Barry, J. F.; Turner, M. J.; Schloss, J. M.; Glenn, D. R.; Song, Y.; Lukin, M. D.; Park, H.; Walsworth, R. L. Optical magnetic detection of single-neuron action potentials using quantum defects in diamond. *Proc. Natl. Acad. Sci. U. S. A.* **2016**, *113*, 14133−14138.

(2) Turner, M. J.; Langellier, N.; Bainbridge, R.; Walters, D.; Meesala, S.; Babinec, T. M.; Kehayias, P.; Yacoby, A.; Hu, E.; Lončar, M.; et al. Magnetic Field Fingerprinting of Integrated Circuit Activity with a Quantum Diamond Microscope. *Phys. Rev. Appl.* **2020**, *14*, 014097.

(3) Thiel, L.; Rohner, D.; Ganzhorn, M.; Appel, P.; Neu, E.; Müller, B.; Kleiner, R.; Koelle, D.; Maletinsky, P. Quantitative nanoscale vortex imaging using a cryogenic quantum magnetometer. *Nat. Nanotechnol.* **2016**, *11*, 677−681.

(4) Tetienne, J.-P.; Hingant, T.; Martínez, L. J.; Rohart, S.; Thiaville, A.; Diez, L. H.; Garcia, K.; Adam, J.-P.; Kim, J.-V.; Roch, J.-F.; et al. The nature of domain walls in ultrathin ferromagnets revealed by scanning nanomagnetometry. *Nat. Commun.* **2015**, *6*, 6733.

(5) Du, C.; Van der Sar, T.; Zhou, T. X.; Upadhyaya, P.; Casola, F.; Zhang, H.; Onbasli, M. C.; Ross, C. A.; Walsworth, R. L.; Tserkovnyak, Y.; et al. Control and local measurement of the spin chemical potential in a magnetic insulator. *Science* **2017**, *357*, 195−198.

(6) Ku, M. J.; Zhou, T. X.; Li, Q.; Shin, Y. J.; Shi, J. K.; Burch, C.; Anderson, L. E.; Pierce, A. T.; Xie, Y.; Hamo, A.; et al. Imaging viscous flow of the Dirac fluid in graphene. *Nature* **2020**, *583*, 537−541.

(7) Barry, J. F.; Schloss, J. M.; Bauch, E.; Turner, M. J.; Hart, C. A.; Pham, L. M.; Walsworth, R. L. Sensitivity optimization for NV-diamond magnetometry. *Rev. Mod. Phys.* **2020**, *92*, 015004.

(8) Acosta, V.; Bauch, E.; Jarmola, A.; Zipp, L.; Ledbetter, M.; Budker, D. Broadband magnetometry by infrared-absorption detection of nitrogen-vacancy ensembles in diamond. *Appl. Phys. Lett.* **2010**, *97*, 174104.

(9) Dumeige, Y.; Chipaux, M.; Jacques, V.; Treussart, F.; Roch, J.-F.; Debuisschert, T.; Acosta, V. M.; Jarmola, A.; Jensen, K.; Kehayias, P.; Budker, D. Magnetometry with nitrogen-vacancy ensembles in diamond based on infrared absorption in a doubly resonant optical cavity. *Phys. Rev. B: Condens. Matter Mater. Phys.* **2013**, *87*, 155202.

(10) Chatzidrosos, G.; Wickenbrock, A.; Bougas, L.; Leefer, N.; Wu, T.; Jensen, K.; Dumeige, Y.; Budker, D. Miniature Cavity-Enhanced Diamond Magnetometer. *Phys. Rev. Appl.* **2017**, *8*, 044019.

(11) Bougas, L.; Wilzewski, A.; Dumeige, Y.; Antypas, D.; Wu, T.; Wickenbrock, A.; Bourgeois, E.; Nesladek, M.; Clevenson, H.; Braje, D.; et al. On the possibility of miniature diamond-based magnetometers using waveguide geometries. *Micromachines* **2018**, *9*, 276.

(12) Jensen, K.; Leefer, N.; Jarmola, A.; Dumeige, Y.; Acosta, V. M.; Kehayias, P.; Patton, B.; Budker, D. Cavity-enhanced room-temperature magnetometry using absorption by nitrogen-vacancy centers in diamond. *Phys. Rev. Lett.* **2014**, *112*, 160802.

(13) Gao, H.; McMahon, J.; Lee, M.; Henzie, J.; Gray, S.; Schatz, G.; Odom, T. Rayleigh anomaly-surface plasmon polariton resonances in palladium and gold subwavelength hole arrays. *Opt. Express* **2009**, *17*, 2334−2340.

(14) Steele, J.; Moran, C.; Lee, A.; Aguirre, C.; Halas, N. Metallodielectric gratings with subwavelength slots: Optical properties. *Phys. Rev. B: Condens. Matter Mater. Phys.* **2003**, *68*, 205103.

(15) Acosta, V.; Jarmola, A.; Bauch, E.; Budker, D. Optical properties of the nitrogen-vacancy singlet levels in diamond. *Phys. Rev. B: Condens. Matter Mater. Phys.* **2010**, *82*, 201202.

(16) Shalaginov, M. Y.; Bogdanov, S. I.; Lagutchev, A. S.; Kildishev, A. V.; Boltasseva, A.; Shalaev, V. M. On-Chip Single-Layer Integration of Diamond Spins with Microwave and Plasmonic Channels. *ACS Photonics* **2020**, *7*, 2018−2026.

(17) Ibrahim, M. I.; Foy, C.; Englund, D. R.; Han, R. High-Scalability CMOS Quantum Magnetometer With Spin-State Excitation and Detection of Diamond Color Centers. *IEEE J. Solid-State Circuits* **2021**, *56*, 1001−1014.

(18) Zhang, H.; Arai, K.; Belthangady, C.; Jaskula, J.-C.; Walsworth, R. L. Selective addressing of solid-state spins at the nanoscale via magnetic resonance frequency encoding. *Npj Quantum Inf.* **2017**, *3*, 31.

(19) Choy, J. T.; Bulu, I.; Hausmann, B. J.; Janitz, E.; Huang, I.-C.; Lončar, M. Spontaneous emission and collection efficiency enhancement of single emitters in diamond via plasmonic cavities and gratings. *Appl. Phys. Lett.* **2013**, *103*, 161101.

(20) Akselrod, G. M.; Argyropoulos, C.; Hoang, T. B.; Cirací, C.; Fang, C.; Huang, J.; Smith, D. R.; Mikkelsen, M. H. Probing the mechanisms of large Purcell enhancement in plasmonic nanoantennas. *Nat. Photonics* **2014**, *8*, 835−840.

(21) Hoang, T. B.; Akselrod, G. M.; Argyropoulos, C.; Huang, J.; Smith, D. R.; Mikkelsen, M. H. Ultrafast spontaneous emission source using plasmonic nanoantennas. *Nat. Commun.* **2015**, *6*, 7788.

(22) Karamlou, A.; Trusheim, M. E.; Englund, D. Metal-dielectric antennas for efficient photon collection from diamond color centers. *Opt. Express* **2018**, *26*, 3341−3352.

(23) Bogdanov, S.; Shalaginov, M. Y.; Akimov, A.; Lagutchev, A. S.; Kapitanova, P.; Liu, J.; Woods, D.; Ferrera, M.; Belov, P.; Irudayaraj, J.; et al. Electron spin contrast of Purcell-enhanced nitrogen-vacancy ensembles in nanodiamonds. *Phys. Rev. B: Condens. Matter Mater. Phys.* **2017**, *96*, 035146.

(24) De Leon, N. P.; Shields, B. J.; Yu, C. L.; Englund, D. E.; Akimov, A. V.; Lukin, M. D.; Park, H. Tailoring light-matter interaction with a nanoscale plasmon resonator. *Phys. Rev. Lett.* **2012**, *108*, 226803.

(25) Hausmann, B. J. M.; Shields, B. J.; Quan, Q.; Chu, Y.; de Leon, N. P.; Evans, R.; Burek, M. J.; Zibrov, A. S.; Markham, M.; Twitchen, D.; et al. Coupling of NV centers to photonic crystal nanobeams in diamond. *Nano Lett.* **2013**, *13*, 5791−5796.

(26) Jun, Y. C.; Pala, R.; Brongersma, M. L. Strong modification of quantum dot spontaneous emission via gap plasmon coupling in metal nanoslits. *J. Phys. Chem. C* **2010**, *114*, 7269−7273.

(27) Russell, K. J.; Liu, T.-L.; Cui, S.; Hu, E. L. Large spontaneous emission enhancement in plasmonic nanocavities. *Nat. Photonics* **2012**, *6*, 459−462.

(28) Wood, R. W. Anomalous Diffraction Gratings. *Phys. Rev.* **1935**, *48*, 928.

(29) Rayleigh, L., III Note on the remarkable case of diffraction spectra described by Prof. Wood. *London Edinburgh Philos. Mag. J. Sci.* **1907**, *14*, 60−65.

(30) Hart, C. A.; Schloss, J. M.; Turner, M. J.; Scheidegger, P. J.; Bauch, E.; Walsworth, R. L. N-V-Diamond Magnetic Microscopy Using a Double Quantum 4-Ramsey Protocol. *Phys. Rev. Appl.* **2021**, *15*, 044020.

(31) Ulbricht, R.; Loh, Z.-H. Excited-state lifetime of the NV^- infrared transition in diamond. *Phys. Rev. B: Condens. Matter Mater. Phys.* **2018**, *98*, 094309.

(32) Sun, J.; Timurdogan, E.; Yaacobi, A.; Hosseini, E. S.; Watts, M. R. Large-scale nanophotonic phased array. *Nature* **2013**, *493*, 195−199.

(33) Bogaerts, W.; Pérez, D.; Capmany, J.; Miller, D. A.; Poon, J.; Englund, D.; Morichetti, F.; Melloni, A. Programmable photonic circuits. *Nature* **2020**, *586*, 207−216.

(34) Rossman, U.; Tenne, R.; Solomon, O.; Kaplan-Ashiri, I.; Dadosh, T.; Eldar, Y. C.; Oron, D. Rapid quantum image scanning microscopy by joint sparse reconstruction. *Optica* **2019**, *6*, 1290−1296.

(35) Grace, M. R.; Dutton, Z.; Ashok, A.; Guha, S. Approaching quantum-limited imaging resolution without prior knowledge of the object location. *J. Opt. Soc. Am. A* **2020**, *37*, 1288−1299.

(36) Howland, G. A.; Dixon, P. B.; Howell, J. C. Photon-counting compressive sensing laser radar for 3D imaging. *Appl. Opt.* **2011**, *50*, 5917−5920.

(37) White, A. G.; Mitchell, J. R.; Nairz, O.; Kwiat, P. G. Interaction-free" imaging. *Phys. Rev. A: At., Mol., Opt. Phys.* **1998**, *58*, 605.

https://doi.org/10.1021/acsphotonics.1c01005
ACS Photonics 2021, 8, 3218−3225

(38) Lemos, G. B.; Borish, V.; Cole, G. D.; Ramelow, S.; Lapkiewicz, R.; Zeilinger, A. Quantum imaging with undetected photons. *Nature* **2014**, *512*, 409−412.
(39) Okamoto, R.; Tokami, Y.; Takeuchi, S. Loss tolerant quantum absorption measurement. *New J. Phys.* **2020**, *22*, 103016.
(40) Balasubramanian, P.; Osterkamp, C.; Chen, Y.; Chen, X.; Teraji, T.; Wu, E.; Naydenov, B.; Jelezko, F. Dc magnetometry with engineered nitrogen-vacancy spin ensembles in diamond. *Nano Lett.* **2019**, *19*, 6681−6686.
(41) Tetienne, J.; Rondin, L.; Spinicelli, P.; Chipaux, M.; Debuisschert, T.; Roch, J.; Jacques, V. Magnetic-field-dependent photodynamics of single NV defects in diamond: an application to qualitative all-optical magnetic imaging. *New J. Phys.* **2012**, *14*, 103033.
(42) Robledo, L.; Bernien, H.; Van Der Sar, T.; Hanson, R. Spin dynamics in the optical cycle of single nitrogen-vacancy centres in diamond. *New J. Phys.* **2011**, *13*, 025013.
(43) Wee, T.-L.; Tzeng, Y.-K.; Han, C.-C.; Chang, H.-C.; Fann, W.; Hsu, J.-H.; Chen, K.-M.; Yu, Y.-C. Two-photon excited fluorescence of nitrogen-vacancy centers in proton-irradiated type Ib diamond. *J. Phys. Chem. A* **2007**, *111*, 9379−9386.
(44) Meng, Z.; Lang, T.; Wessel, S.; Assaad, F.; Muramatsu, A. Quantum spin liquid emerging in two-dimensional correlated Dirac fermions. *Nature* **2010**, *464*, 847−851.
(45) Takagi, H.; Takayama, T.; Jackeli, G.; Khaliullin, G.; Nagler, S. E. Concept and realization of Kitaev quantum spin liquids. *Nat. Rev. Phys.* **2019**, *1*, 264−280.
(46) Cappellaro, P.; Lukin, M. D. Quantum correlation in disordered spin systems: Applications to magnetic sensing. *Phys. Rev. A: At., Mol., Opt. Phys.* **2009**, *80*, 032311.
(47) Choi, S.; Yao, N. Y.; Lukin, M. D. Quantum metrology based on strongly correlated matter. *arXiv*, arXiv:1801.00042, 2017.

https://doi.org/10.1021/acsphotonics.1c01005
ACS Photonics 2021, 8, 3218−3225